Front. Mech. Eng. 2012, 7(2): 150–162
DOI 10.1007/s11465-012-0325-4

RESEARCH ARTICLE

Abdelbadiâ CHAKER, Abdelfattah MLIKA, Med Amine LARIBI, Lotfi ROMDHANE, Saïd ZEGHLOUL

Synthesis of spherical parallel manipulator for dexterous medical task

Abstract This paper deals with the design and the analysis of a spherical parallel manipulator (SPM) for a haptic minimally invasive surgery application. First the medical task was characterized with the help of a surgeon who performed a suture technique called anastomosis. A Vicon system was used to capture the motion of the surgeon, which yielded the volume swept by the tool during the anastomosis operation. The identified workspace can be represented by a cone with a half vertex angle of 26°. A multi objective optimization procedure based on genetic algorithms was then carried out to find the optimal SPM. Two criteria were considered, i.e., task workspace and mechanism dexterity. The optimized SPM was then analyzed to determine the error on the orientation of the end effector as a function of the manufacturing errors of the different links of the mechanism.

Keywords spherical parallel manipulator (SPM), anastomosis, haptic, motion capture, optimization, workspace, dexterity, genetic algorithm, manufacturing errors

1 Introduction

We focus in this paper on the design of a haptic interface for medical applications, especially minimally invasive surgery (MIS). This technique reduces pain, leads to brief hospital stays and shorter rehabilitation time. In this context, the desired device should provide the surgeon with natural eye-hand-coordination, dexterity, precision and force feedback for tele operation.

Received January 3, 2012; accepted March 1, 2012

Abdelbadiâ CHAKER, Abdelfattah MLIKA, Lotfi ROMDHANE (✉)
Laboratoire de Mécanique de Sousse, Ecole Nationale d'Ingénieurs de Sousse Université de Sousse, Sousse, Tunisia
E-mail: lotfi.romdhane@gmail.com

Abdelbadiâ CHAKER, Med Amine LARIBI, Saïd ZEGHLOUL
Institut PPRIME, CNRS, Université de Poitiers—ENSMA, UPR 3346, Poitiers, France

The spherical parallel architecture represents an interesting alternative for applications with a fixed center of rotation as is the case of the MIS. Different varieties of this mechanism have been studied before. These studies covered a wide range of features such as workspace analysis [1–3], kinematic analysis [4–6], optimization of design parameters [7], singularity analysis [8,9] and dexterity [10].

Another characteristic of the 3-RRR spherical parallel manipulator (SPM) is its degree of overconstraints. Indeed, several studies in the literature showed that the 3-RRR is an overconstrained mechanism [11–13]. This characteristic yields high rigidity and hence a better precision. However, the mounting of the mechanism and its precision can be affected by the manufacturing errors of its links. One way to go around this problem is to remove the source of overconstraints by modifying the nature of the joints [11,14]. The 3-RCC SPM is one of the proposed non overconstrained mechanisms. The added translational motion along the axis of the *C* joints can help the mounting of the mechanism without the need to deform the links. In this case, Al-Widyan et al. [13] evaluated through a stochastic method the translational displacement of each cylindrical joint in the 3-RCC architecture.

While these small displacements allow the mounting of the mechanism without the need to deform the links, they can yield errors and reduce the rigidity of the mechanism compared to the overconstrained case.

In this paper, we prefer maintaining the overconstraints in the 3-RRR mechanism and stochastically evaluate the error on the orientation of the end effector as a result of the manufacturing errors of the different links of the mechanism.

Section 2 presents an experimental description of the anastomosis task. A motion capture system was used to acquire the motion of markers mounted on the tools used by an expert during a suture operation. The workspace necessary for this task is then determined experimentally. Section 3 presents the kinematic analysis and a workspace representation of the SPM. An optimization procedure, using genetic algorithms, is then used, in Sect. 4, to

determine the optimum design parameters of the robot yielding the required workspace and providing a high dexterity. Section 5 presents the optimal manipulator and details the effect of dexterity as a criterion in the optimization procedure. Section 6 takes advantage of screws of small displacements method to represent and study the effect of manufacturing errors of the different links of the mechanism on the orientation error of the end effector. Section 7 concludes this paper.

2 Characterization of the medical task

2.1 Experimental protocol

The first step, in the design of such systems, is to identify the nature of the movements required to perform a mini invasive surgery. One of the main tasks encountered in this procedure is the suturing operation. An experimented surgeon was asked to perform this task on a training station in order to analyze the motion and the technique he uses. Figure 2 presents the experimentation scene with the practitioner manipulating the tools (a clamp and a needle holder) on the Pelvis Trainer station. The task consists on the surgical union of two hollow organs or parts that are normally separate, called anastomosis. Experiments were then applied on a ruptured aortic vessel. The technique is made of three phases: the first one consists of suturing the back hemisphere, which is the most difficult to reach. The second step is to suture the front hemisphere and finally performing a triple knot. Figure 1 shows these three phases on a prosthetic aorta.

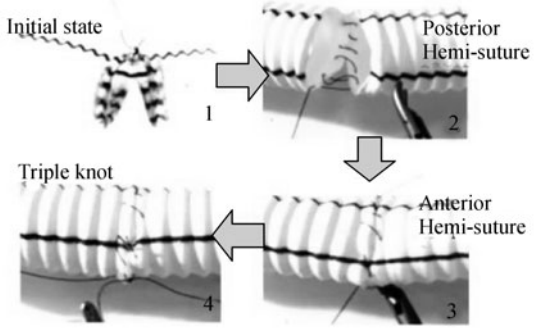

Fig. 1 Anastomosis phases

2.2 Motion capture

The aim is to characterize the motion of the expert hand during a mini invasive surgery. Our motion capture method is based on the experience of the biomechanics community especially for the choice of marker sets and segment reference definition [15]. Computer graphics focus on the use of motion capture and synthesis movement to generate three-dimensional realistic movements for virtual models.

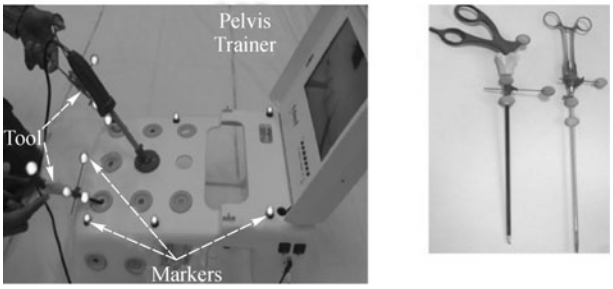

Fig. 2 Experimental setup (Pelvis Trainer + tools)

A set of 28 markers were fixed on the practitioner hand and the surgical tools. A motion capture system made of 10 high speed cameras was used to track and record the position of these markers. The tools have to go through small holes, simulating the skin incisions, and the movements were basically rotations around the incision point and a translation along the axis of the tool.

The recorded kinematics data is based on the use of the Vicon Nexus motion capture system. Using Nexus software, we identify the three coordinates of each marker at every moment, in the reference coordinates system, by combining coordinates in every camera reference. The data are typically a set of coordinates of each marker as a function of time.

2.3 Data analysis

At the end of the surgical operation, the motion capture system stores all the recorded data. These data are then analyzed to identify the kinematics of the performed movements. Figure 3 shows the reconstructed model using the Software Nexus in the MOTION CAPTURE and the expert performing the anastomosis.

These data were used to evaluate the size of the workspace within which the tool was moving. We limit our workspace to the two rotations of the axis of the tool and we discard, as a first analysis, the self-rotation. Since the tool has to go always through the hole, we decided to evaluate the size workspace through the calculation of the maximum angle of the cone generated by the axis of the tool. Figure 4 contains two cones, one corresponds to the clamp with an angle of 17° and the second one is for the needle holder, which has 26° as the angle of the cone.

Each cone vertex coincides with the corresponding hole in the ‘pelvis trainer’, which is a simulation of the incision in the human body. Besides the rotation, each tool has also a translation motion along the axis of the cone.

This last movement will not be considered here and we will limit the study to only the rotation. We notice that it can happen that the axes of the tools intersect, which is predictable since they both cooperate to perform the task. This study highlights the complexity of the surgeon movements during anastomosis.

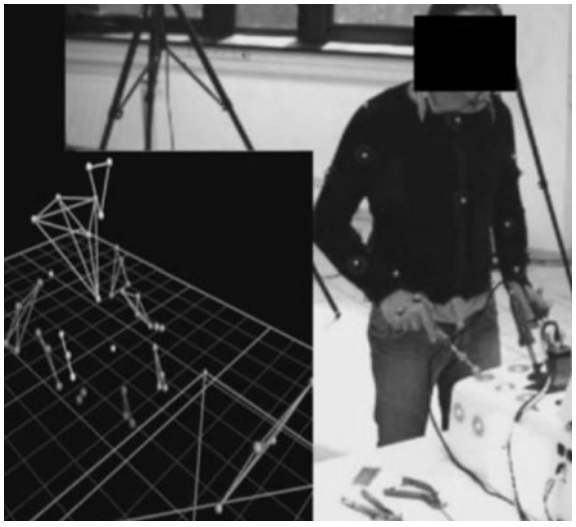

Fig. 3 Motion reconstitution

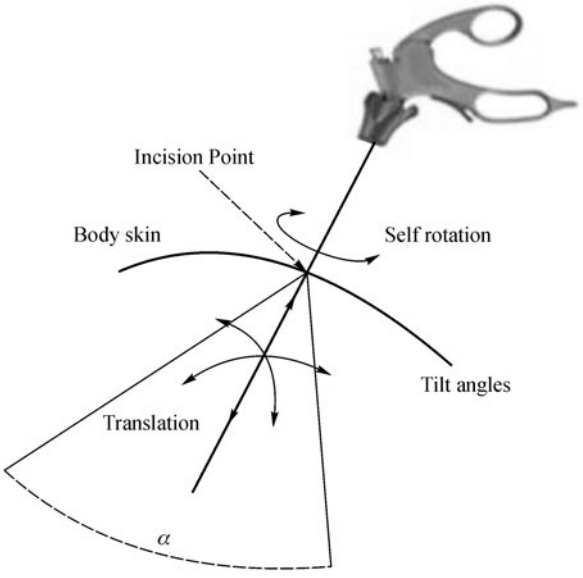

Fig. 5 DOF in MIS motion

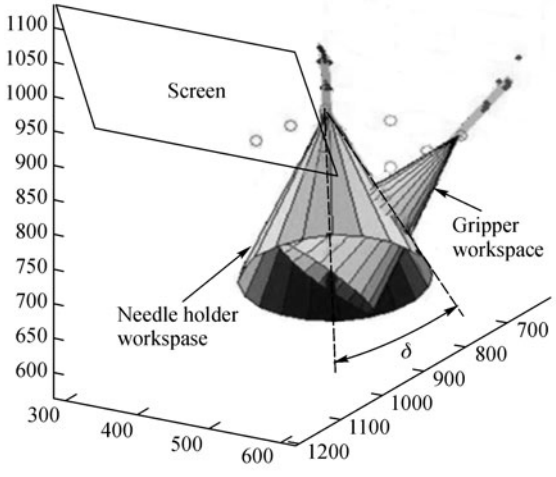

Fig. 4 Tools workspace resulting from experimentations

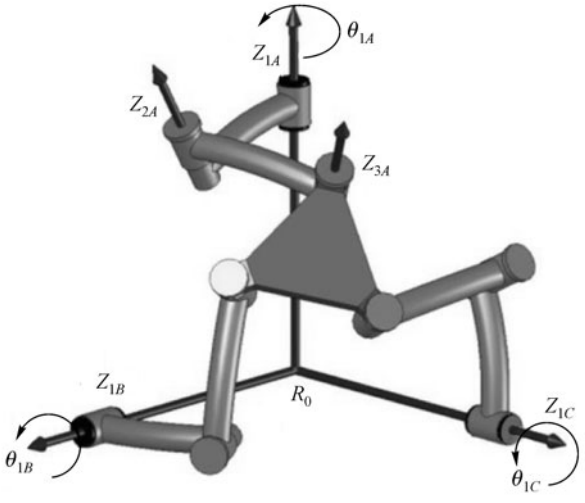

Fig. 6 Proposed architecture

In conclusion, each tool has to perform three movements of rotation and one movement of translation presented in Fig. 5. Two rotations are used to orient the axis of the cone and the third one is a self-rotation. The translation is also along the axis of the cone.

3 Proposed architecture of SPM

Figure 6 depicts a CAD model of the proposed architecture for the haptic system. Figure 7 shows the manufactured prototype of the system.

It consists of a spherical parallel mechanism providing the three rotations needed to the MIS application. This choice is motivated by the fact that the output motion of this type of robots is generated around a fixed center of rotation that coincides in reality with the incision on the patient body. Figure 8 shows the CAD model of the system with the surgical tool mounted on the platform. The center of rotation corresponds to the incision point on the patient body and the cone has the same size as the one determined by the motion capture system.

In fact, the workspace of the structure is the intersection of three spherical caps generated each by a separate serial leg. Moreover, parallel robots are known to have high rigidity and precision along with a low inertia.

The mechanism is composed of three pairs of links that connect the base to the platform. Each of these pairs is formed by a proximal link joined to the base and a distal one joined to the platform. The joints are all revolute joints and all axes intersect in a single point.

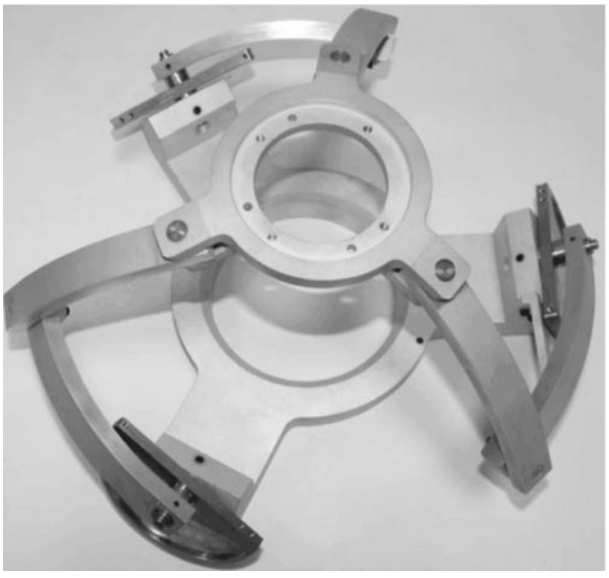

Fig. 7 Prototype of the SPM

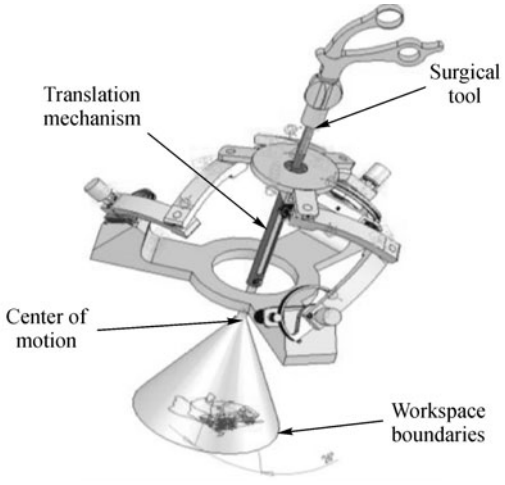

Fig. 8 CAD model of the proposed device

The axes of the base frame of the structure $\mathcal{R}_0$ meet the axes of the three base joints. Thus, the center of rotation represents the vertex of a pyramid that inscribes the structure. The three revolute joints with the base are actuated. These motors will be responsible of generating the force feedback to the practitioner by resisting the motion proportionally to the forces acting on the tool tip on the slave robot. The fourth degree of freedom, required by the task, is a translation along the z-axis of the platform. This DOF is decoupled from rotations and does not affect the orientation of the device, and it will not be considered in this work.

4 Kinematic analysis

The spherical parallel mechanism is characterized by the fact that all the joint axes are intersecting in one point. The three legs are identical and the actuated joint axes are located along the x, y and z axes, respectively. The workspace of the platform is then the intersection of the workspaces of three legs considered each as a 3-DOF spherical serial kinematic chain.

4.1 Forward displacement of the SPM

The motion of the SPM is generated by only revolute joints. The position of the three identical legs A, B, C can then be described by the vector $\boldsymbol{q}_A$:

$$\boldsymbol{q}_A = [\theta_{1k},\theta_{2k},\theta_{3k}]^{\mathrm{T}},\ (k = A,B,C). \tag{1}$$

The operational vector of angles $[\psi,\theta,\varphi]^{\mathrm{T}}$, are the three $ZXZ-$Euler angles of the platform, representing the orientation of the platform with respect to the base. Using successive rotations one can find the orientation of the platform as a function of the different rotations of the active joints. Figure 9 describes the parameters of a serial leg. The proximal link is defined by the angle α that separate the axis of the actuated joint and the axis of intermediate joint. The distal link is defined by the angle β that separate the axis of the intermediate joint and the axis of platform joint. The angle γ defines the dimension of the platform.

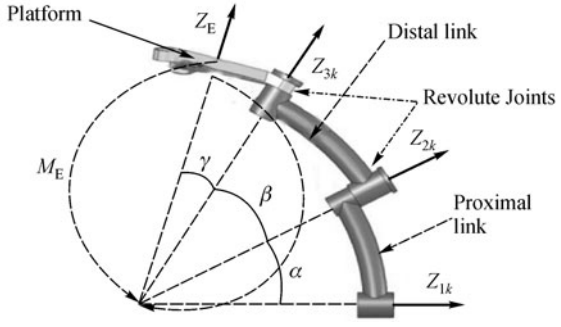

Fig. 9 One leg geometric parameters

The geometric model can be written in a matrix form as a relation between the representations of platform orientation using joints parameters and Euler parameters

$$Rot(\boldsymbol{Z}_{1k},\theta_{1k})\cdot Rot(\boldsymbol{X}_{2k},\alpha)\cdot Rot(\boldsymbol{Z}_{2k},\theta_{2k})\cdot Rot(\boldsymbol{X}_{3k},\beta)$$

$$\cdot Rot(\boldsymbol{Z}_{3k},\theta_{3k})\cdot Rot(\boldsymbol{X}_E,\gamma)$$

$$= Rot(\boldsymbol{Z},\psi)\cdot Rot(\boldsymbol{X}',\theta)\cdot Rot(\boldsymbol{Z}_E,\varphi), \tag{2}$$

with

$$\begin{aligned} \boldsymbol{X}_{2k} &= \boldsymbol{Z}_{1k}\times\boldsymbol{Z}_{2k},\\ \boldsymbol{X}_{3k} &= \boldsymbol{Z}_{2k}\times\boldsymbol{Z}_{3k},\\ \boldsymbol{X}_E &= \boldsymbol{Z}_{3k}\times\boldsymbol{Z}_E, \end{aligned} \tag{3}$$

and $k = A$, B, C denotes the three legs.

This matrix equation can be reduced to three scalar equations, written as

$$\begin{cases} \psi = f_1(\theta_{1A},\theta_{2A},\theta_{3A}), \\ \theta = f_2(\theta_{1A},\theta_{2A},\theta_{3A}), \\ \varphi = f_3(\theta_{1A},\theta_{2A},\theta_{3A}). \end{cases} \tag{4}$$

The inverse model, however, is easier to write. For leg $k(k = A,B,C)$, one can write

$$\boldsymbol{Z}_{2k} \cdot \boldsymbol{Z}_{3k} = \cos\beta, \tag{5}$$

with

$$\boldsymbol{Z}_{2k} = Rot(\boldsymbol{Z}_{1k},\theta_{1k}) \cdot Rot(\boldsymbol{X}_{2k},\alpha) \cdot \boldsymbol{Z}_{1k}, \tag{6}$$

$$\boldsymbol{Z}_{3k} = Rot(\boldsymbol{Z}_{1k},\psi) \cdot Rot(\boldsymbol{X}',\theta) \cdot Rot(\boldsymbol{Z}_E,\varphi) \cdot Rot^{-1}(\boldsymbol{X}_E,\gamma) \cdot \boldsymbol{Z}_{1k}. \tag{7}$$

The latter equations can be decoupled to yield the following three scalar equations involving the variables θ_{1k}, ψ, θ, φ:

$$\begin{cases} A_1\cos\theta_{1A} + B_1\sin\theta_{1A} = C_1, \\ A_2\cos\theta_{1B} + B_2\sin\theta_{1B} = C_2, \\ A_3\cos\theta_{1C} + B_3\sin\theta_{1C} = C_3. \end{cases} \tag{8}$$

A_i, B_i and C_i are constant functions of the geometric parameters. Equation (8) have a solution if and only if the following conditions have to be fulfilled simultaneously

$$\begin{cases} CD_i(\alpha,\beta,\gamma,\psi,\theta,\varphi) : \dfrac{C_i^2}{A_i^2 + B_i^2} \leqslant 1, \\ i = 1,2,3. \end{cases} \tag{9}$$

Therefore, for a given orientation of the platform, the constants A_i, B_i and C_i are determined and the actuated joint angles θ_{1k} are the solutions of the three decoupled equations, given by Eq. (8).

For a given self-rotation, φ, the workspace can be represented in the Cartesian workspace as the accessible orientations of the $\boldsymbol{Z}_E$ — vector of the platform. Figure 10(a) shows these orientations for different values of self-rotation φ, where locations of the tip of this vector are represented in the Cartesian reference frame. One can notice that the 'size' of the workspace is reduced when varying the angle φ. Figure 10(b) shows the variation of the workspace as a function of the angle φ in the (ψ,θ) space.

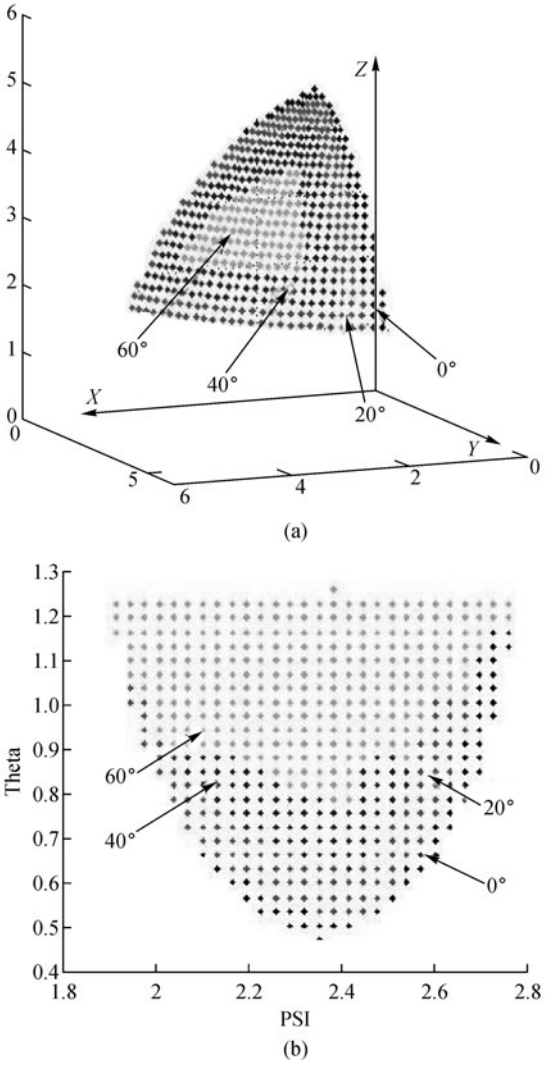

Fig. 10 SPM workspace ($\alpha = 28°$, $\beta = 26°$, $\gamma = 18°$), for $\varphi = \{0°, 20°, 40°, 60°\}$. (a) Cartesian space; (b) (ψ,θ) space

4.2 Kinematic model

The kinematic model can be obtained by differentiating Eq. (5) with respect to time. The obtained equation can be written as

$$\dot{\boldsymbol{Z}}_{2k}\boldsymbol{Z}_{3k} + \boldsymbol{Z}_{2k}\dot{\boldsymbol{Z}}_{3k} = 0, \tag{10}$$

with

$$\dot{\boldsymbol{Z}}_{2k} = \dot{\theta}_{1k}\boldsymbol{Z}_{1k} \times \boldsymbol{Z}_{2k}, \tag{11}$$

and

$$\dot{\boldsymbol{Z}}_{3k} = \boldsymbol{\omega} \times \boldsymbol{Z}_{3k},$$

$\boldsymbol{\omega}$ is the angular velocity of the end effector.

We get

$$\dot{\theta}_{1k}\boldsymbol{Z}_{1k} \times \boldsymbol{Z}_{2k} \cdot \boldsymbol{Z}_{3k} = -\boldsymbol{Z}_{2k} \cdot \boldsymbol{\omega} \times \boldsymbol{Z}_{3k}, \tag{12}$$

$$\boldsymbol{Z}_{1k} \times \boldsymbol{Z}_{2k} \cdot \boldsymbol{Z}_{3k}\dot{\theta}_{1k} = -\boldsymbol{Z}_{3k} \times \boldsymbol{Z}_{2k} \cdot \boldsymbol{\omega}. \tag{13}$$

For the whole manipulator and in a matrix form, we can write

$$\boldsymbol{B}\dot{\boldsymbol{q}} = \boldsymbol{A}\boldsymbol{\omega}, \tag{14}$$

where $\boldsymbol{B}$ is a 3×3 diagonal matrix defined as follows:

$$\boldsymbol{B}=\begin{bmatrix}\boldsymbol{Z}_{1B}\times\boldsymbol{Z}_{2B}\times\boldsymbol{Z}_{3B} & & \\ & \boldsymbol{Z}_{1B}\times\boldsymbol{Z}_{2B}\times\boldsymbol{Z}_{3B} & \\ & & \boldsymbol{Z}_{1C}\times\boldsymbol{Z}_{2C}\times\boldsymbol{Z}_{3C}\end{bmatrix}, \tag{15}$$

and

$$\dot{\boldsymbol{q}}=\left[\dot{\theta}_{1A}\dot{\theta}_{1B}\dot{\theta}_{1C}\right]^{\mathrm{T}}, \tag{16}$$

$$\boldsymbol{A}=\begin{bmatrix}(\boldsymbol{Z}_{3A}\times\boldsymbol{Z}_{2A})^{\mathrm{T}}\\(\boldsymbol{Z}_{3B}\times\boldsymbol{Z}_{2B})^{\mathrm{T}}\\(\boldsymbol{Z}_{3C}\times\boldsymbol{Z}_{2C})^{\mathrm{T}}\end{bmatrix}, \tag{17}$$

$$\boldsymbol{\omega}=\begin{bmatrix}\dot{\theta}\cos\psi+\dot{\varphi}\sin\theta\sin\psi\\ \dot{\theta}\sin\psi-\dot{\varphi}\sin\theta\cos\psi\\ \dot{\psi}+\dot{\varphi}\cos\theta\end{bmatrix}. \tag{18}$$

4.3 Dexterity

Suturing and knot-tying tasks during endoscopic surgery require a high level of precision and dexterity. Therefore, it is of utmost importance that the proposed robot maintains a certain level of dexterity over its workspace. Dexterity is indeed a measure reflecting the amplification of error due to the kinematic and statistic transformations between the joints and the Cartesian space. Several criteria were proposed in the literature to quantify the dexterity of robot manipulators. In this work, we propose the most used one, which is the condition number of the Jacobean matrix that describes the overall kinematic behavior of a robot [16]. The problem of non-homogeneity of the Jacobean matrix is not encountered in our case since the SPM has only orientation degrees of freedom. Therefore, the condition number can be a reliable measure of this dexterity. The kinematic model can be written as

$$\boldsymbol{\omega}=\boldsymbol{J}\dot{\boldsymbol{q}}=\boldsymbol{A}^{-1}\boldsymbol{B}\dot{\boldsymbol{q}}. \tag{19}$$

The condition number of the matrix $\boldsymbol{J}$ isdefined as

$$k(\boldsymbol{J})=\|\boldsymbol{J}\|\left\|\boldsymbol{J}^{-1}\right\|. \tag{20}$$

Using the 2-norm defined as the square root of the largest eigen value of matrix $\boldsymbol{J}\boldsymbol{J}^{-1}$, the condition number of the matrix $\boldsymbol{J}$ is then the ratio of the largest singular value of $\boldsymbol{J}$ to the smallest

$$k(\boldsymbol{J})=\frac{\sigma_{\max}}{\sigma_{\min}}. \tag{21}$$

The condition number can also be a measure of how far the robot is from singularity. Indeed, in haptic devices it is of most importance to be as far as possible from singularity for the system to function correctly.

It is not easy to detail the analytical expression of the condition number. Hence, we should calculate it numerically for different given poses of the platform. The smallest possible value that we can have is 1. This corresponds to an isotropic pose of the manipulator.

5 Synthesis of the spherical parallel manipulator

Dexterity and workspace of the SPM where detailed in the previous section. These two properties will serve to identify the optimal manipulator for the anastomosis application. The first criterion to satisfy is to find the spherical parallel robot having the smallest workspace containing the specified workspace determined experimentally. The second one is to have the maximum dexterity on this workspace which guarantees the necessary handling accuracy.

5.1 Workspace modeling

The workspace of interest is an orientation workspace defined by the set of Euler angles ψ, θ and φ, which are reachable by the mobile platform of the robot. The prescribed workspace is a conical domain that delimits the accessible orientations of the surgical tool axis. This cone can be easily modeled in the Cartesian space as follows:

$$\boldsymbol{I}\cdot\boldsymbol{Z}_E=\cos\delta, \tag{22}$$

with

$\boldsymbol{I}=\frac{1}{\sqrt{3}}[1\ 1\ 1]^{\mathrm{T}}$ a unit vector defining the axis of the cone

$$\boldsymbol{Z}_E=\begin{bmatrix}\sin\psi\sin\theta\\ -\cos\psi\sin\theta\\ \cos\theta\end{bmatrix}, \tag{23}$$

and δ the half vertex angle of the cone. Equation (22) can be written as

$$(\sin\psi-\cos\psi)\sin\theta+\cos\theta=\sqrt{3}\cos\delta. \tag{24}$$

For $\psi\in[-\pi\ \pi]$, solving Eq. (24) leads to (ψ,θ) couples describing the desired cone detailed as follow:

$$\sqrt{a^2+b^2}\sin(\theta+\alpha)=c, \tag{25}$$

where

$$a = \sin\psi - \cos\psi,$$
$$b = 1, \tag{26}$$
$$c = \sqrt{3}\cos\delta.$$

$$\alpha = \begin{cases} \operatorname{atan}\left(\dfrac{b}{a}\right), & \text{if } a \geqslant 0, \\ \operatorname{atan}\left(\dfrac{b}{a}\right) + \pi, & \text{if } a < 0, \end{cases} \tag{27}$$

$$\theta = -\alpha + \arcsin\left(\frac{c}{\sqrt{a^2 + b^2}}\right), \tag{28}$$

Figure 11 shows a graphical representation of the cone characterized by N 'points' $p_j(\psi_j,\theta_j,\varphi_j)$, an angle and an axis I.

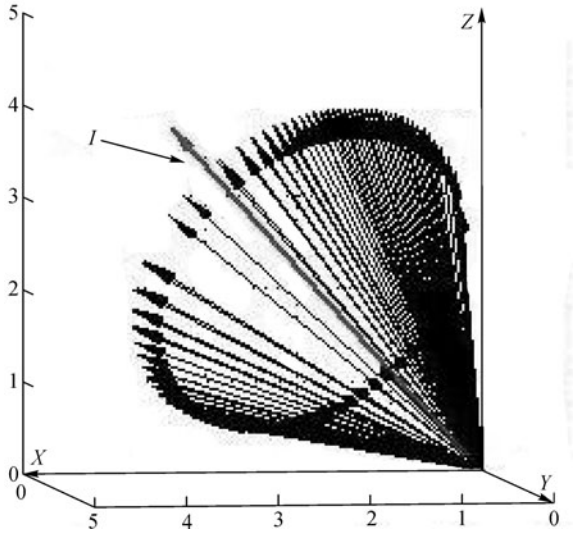

Fig. 11 Prescribed workspace in Cartesian space for $N = 200$

During the optimization process, a security distance was adopted on the desired workspace. This allows us to avoid serial singularities that occur when det ($\boldsymbol{B}$) = 0. The corresponding configurations for these singularities exist on the boundary of the workspace. The vertex angle of the target cone become then $\delta + \varepsilon$. ε is the a security angle chosen to be 4 degrees.

The objective function is a representation of the optimization problem to minimize. It is one of the key elements of genetic algorithm because it determines whether or not a given potential solution will contribute to the next generation through the reproduction process. The Fitness function should be able to provide a good measure of the quality of the solution and should differentiate between the performances of different manipulators. It also associates our two adopted criteria, which are the optimal workspace and the maximum dexterity. This problem can be then stated as follows:

Minimize F_2 and F_3

Subject to

$$CD_i(\boldsymbol{V},P_j) : \frac{C_i^2}{A_i^2 + B_i^2} \leqslant 1 (i = 1,2,3) \ \Big(\text{Eq.}(8)\Big),$$

where $\boldsymbol{V} = [\alpha,\beta,\gamma]$ is the design vector and $P_j(\psi_j,\theta_j,\varphi_j)$ a given orientation of the platform.

This constraint can be handled using a penalty function F_1, defined as follow:

$$F_1 = \sum_{j=1}^{N}\sum_{i=1}^{3}\chi_i(\boldsymbol{V},P_j). \tag{29}$$

where

$$\chi_i(\boldsymbol{V},P_j) = \begin{cases} 0, & \text{if } CD_i \leqslant 1, \\ cf, & \text{if } CD_i > 1, \end{cases} \tag{30}$$

where, cf is a large positive constant.

$F_1 = 0$ means that all the points, defining the desired volume, are contained within the workspace of the spherical parallel manipulator.

The optimization problem becomes

Minimize $F_1 + F_2$ and $F_1 + F_3$.

Before defining F_2 and F_3, we introduce the power of a point functions $f_2(Y,P_j)$ and $f_3(Y,P_j)$, which evaluate, respectively, the distance of the chosen 'point' P_j from the obtained workspace and the dexterity of the mechanism [17,18]. These two functions are determined as follows:

$$f_2(V,P_j) = \sum_{i=1}^{3}\left|\frac{C_i^2(\boldsymbol{V},P_j)}{A_i^2(Y,P_j) + B_i^2(Y,P_j)}\right|, \tag{31}$$

$$f_3(\boldsymbol{V},P_j) = \sum_{i=1}^{3}k(\boldsymbol{V},P_j). \tag{32}$$

$A_i(\boldsymbol{V},P_j)$, $B_i(\boldsymbol{V},P_j)$, and $C_i(\boldsymbol{V},P_j)$ are given by Eq (8). $k(\boldsymbol{V},P_j)$ is the condition number calculated at the 'point' $P_j(\psi_j,\theta_j,\varphi_j)$.

The sum of the distances of all the points represents F_2. When F_2 and F_3 are minimal, we get the robot having the closest workspace to the desired one with a maximum dexterity distribution.

F_2 and F_3 are then given by

$$F_2 = \sum_{j=1}^{N}f_2(\boldsymbol{V},P_j)\sum_{i=1}^{N}\sum_{i=1}^{3}\left|\frac{C_i^2(\boldsymbol{V},P_j)}{A_i^2(\boldsymbol{V},P_j) + \Big(B_i^2(\boldsymbol{V},P_j)\Big)}\right|, \tag{33}$$

$$F_3 = \sum_{j=1}^{N} f_3(\boldsymbol{V},P_j) = \sum_{j=1}^{N}\sum_{i=1}^{3} k(\boldsymbol{V},P_j), \qquad (34)$$

where N is the number of chosen 'points' P_j.

5.2 Genetic Algorithm

The aim of this section is to develop and to solve the optimization problem of selecting the design variables for the SPM having a specified workspace and the best dexterity distribution. This procedure concerns the geometrical parameters of the architecture, i.e., the links angles represented by the designed vector $\boldsymbol{V} = [\alpha,\beta,\gamma]$.

The proposed approach is based on a real coded genetic algorithm (GA). In order to have large intervals of variation for the parameters to be optimized, we run the algorithm on a wide range of values detailed as follows:

$$\alpha \in [20^\circ\ 75^\circ],\ \beta \in [20^\circ\ 75^\circ],\ \gamma \in [0^\circ\ 45^\circ]. \qquad (35)$$

Initially the algorithm generates 500 sets of different design parameters as the first parent generation. Then the three standard genetic operations, i.e., reproduction, crossover, and mutation are performed to produce a new generation. Such procedures are repeated until the chosen number of generations is achieved, or the required accuracy is satisfied. For every manipulator generated, the workspace is calculated and compared to the desired one. The latter operation is performed on 400 different orientations on the workspace boundaries.

5.3 Results and discussion

The optimization is performed using a GA method on 200 generations and 500 individuals. The self-rotation φ of the manipulator was chosen to be $\frac{\pi}{10}$. Initially, we used only the prescribed workspace as a criterion. This led to generate a manipulator yielding the task workspace perfectly. The obtained design vector is

$$\boldsymbol{V} = [43.17^\circ,31.38^\circ,13^\circ]. \qquad (36)$$

The obtained workspace and the desired one represented in the Cartesian space are shown in Fig. 12. We can see clearly the safety space between the cones.

We can observe that the prescribed workspace is completely inside the robot workspace, which means that the robot is able to reach all the necessary orientations to achieve the surgical task. Figure 13 represents the dexterity distribution of the resulting manipulator. We adopted for this representation the inverse of the condition number $\frac{1}{k}$. It is clear that a maximum value of 0.25 for this index is not acceptable and shows the low dexterity of the resulting manipulator.

Therefore, in order to improve this dexterity distribution,

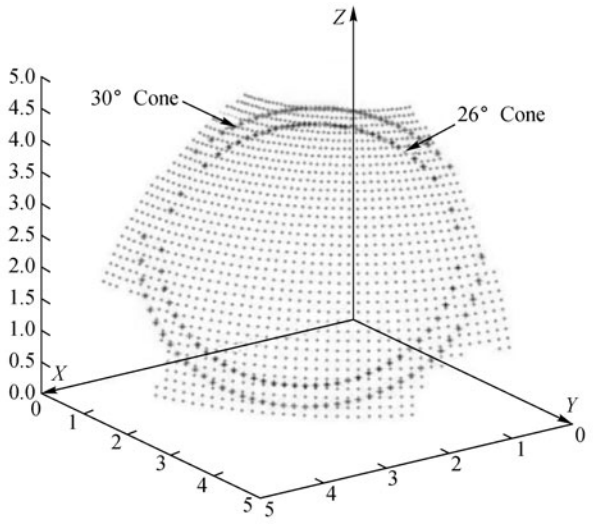

Fig. 12 The workspace of the optimized SPM using the first criterion of workspace

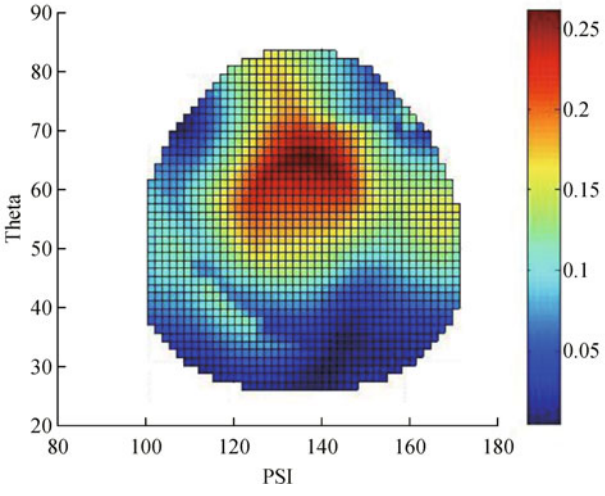

Fig. 13 Dexterity mapping for the workspace optimized SPM

a multi objective optimization, which includes the condition number as a criterion, has been carried out.

The dexterity was then calculated for every manipulator generated by the algorithm. Knowing that the global conditioning index cannot ensure a uniform distribution we adopted the local index. The strategy was then to find the SPM having as much as possible orientations on its workspace with a local conditioning index greater than 0.7. This operation was performed on 37000 orientations on the desired workspace.

The obtained design vector is

$$\boldsymbol{V} = [39.3^\circ,34.1^\circ,18.2^\circ]. \qquad (37)$$

This manipulator provides a significantly better dexterity distribution on the desired workspace, which is necessary for correctly performing the dexterous anasto-

mosis task. We can then have a reasonably uniform dexterity distribution with a global conditioning index of 0.73 and a local index variation from 0.26 to reach a maximum value of 0.95. Figures 14 and 15 represent respectively the workspace and the dexterity distribution of the resulting SPM.

We notice that including dexterity in the optimization process had an effect on the workspace of the optimal manipulator that became larger than the desired one. Optimization with Pareto front could be done to check the possibility of a compromise between these two criteria that may lead to better results.

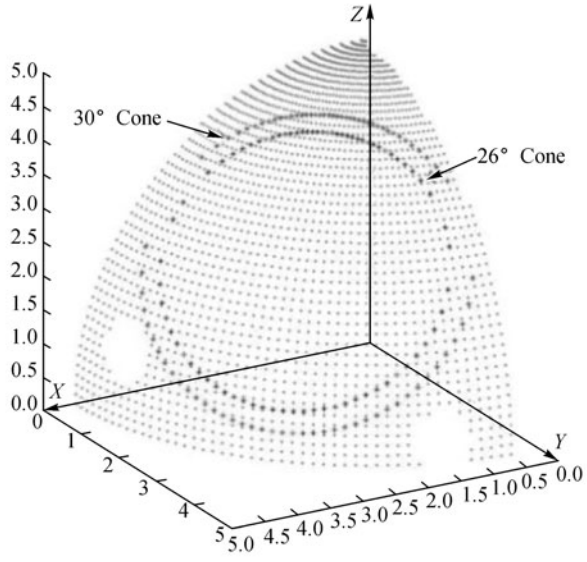

Fig. 14 Workspace of SPM with optimized workspace and dexterity

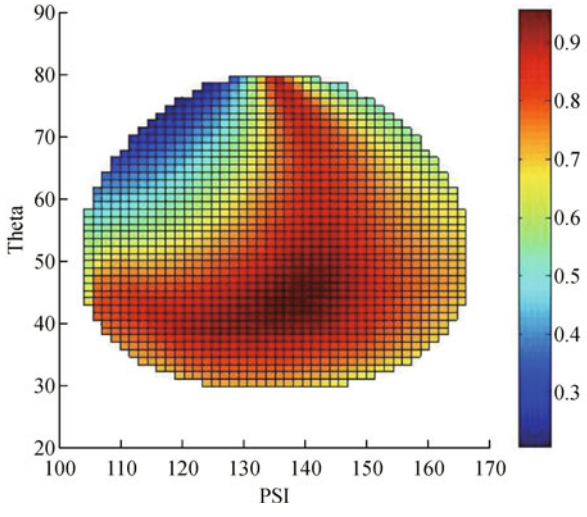

Fig. 15 Dexterity distribution of the resulting SPM

6 Determination of the manufacturing error

The aim of this section is to characterize the orientation errors of the end-effecter of the 3-*RRR* SPM due to the manufacturing errors occurring during parts machining.

The strategy adopted is based on the determination of the maximum acceptable manufacturing errors for a given accuracy of the mechanism. In order to achieve this goal, we evaluated the orientation error of the end effecter generated by a range of manufacturing errors.

The model used in this study assumes that the joints are ideal and that the manufacturing errors can be represented by screws of small motions.

6.1 Screw of manufacturing errors

In the case of an ideal binary *R*-*R* link, a reference frame $R(O,X,Y,Z)$ is attached to the first joint and a second frame $R'(O',X',Y',Z')$ is attached to the second one.

Due to manufacturing errors, the real link replaces the ideal link and the reference frame is replaced by a reference frame $R'^{*}(O'^{*},X'^{*},Y'^{*},Z'^{*})$ (Fig. 16).

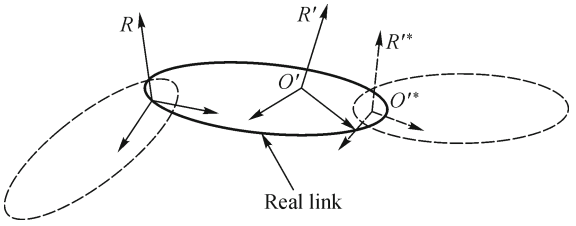

Fig. 16 Real link parameters

Theoretically, the virtual link S^{*} is inserted between the two links S and S' having a joint J. Therefore, joint J becomes between S^{*} and S'. The resulting configuration is presented in Fig. 17. We describe the change between S and S^{*} by a screw of small displacements called $\Im^{s}_{s*}$ and written in the frame R' as

$$\Im^{s}_{s*} = \left\{ \begin{array}{c} \delta\boldsymbol{\rho}^{s}_{s*} \\ \delta\boldsymbol{t}(O'^{*}) \end{array} \right\}_{R'}, \tag{38}$$

where $\delta\boldsymbol{\rho}^{s}_{s*}$ is a small rotation of R'^{*} with respect to R' and $\delta\boldsymbol{t}(O'^{*})$ is a small translation from point O' to point O'^{*}.

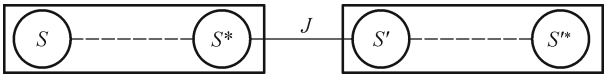

Fig. 17 Model of the joint between link S and link S' taking into account manufacturing errors

Figure 18 depicts the general representation of the SPM considering the insertion of virtual links and details the two closed loops adopted in studying the effects of manufacturing errors.

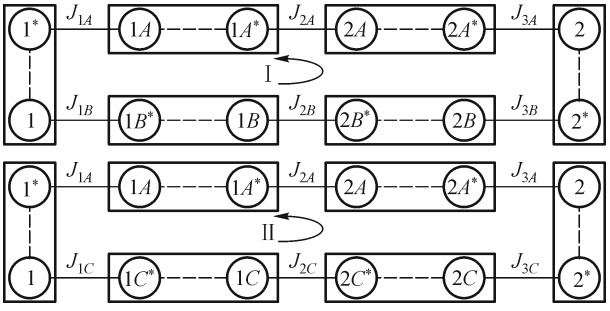

Fig. 18 The two closed loops of the SPM considering the manufacturing errors

6.2 Manufacturing errors for an *R-R* link

Figure 19 presents the studied case of a link connected by two revolute joints (*R*) to adjacent links.

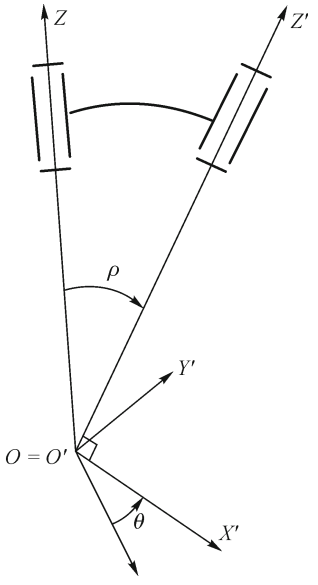

Fig. 19 Ideal link parameters

The first and the second joint axes are respectively $\boldsymbol{Z}$ and $\boldsymbol{Z}'$. The geometry of the link is given by the fixed angle ρ whereas the rotation of the joint is described by the variable θ. The frame R and R' are respectively associated with the first and the second joint.

The screw of the manufacturing errors represents the error on the angle ρ, $\delta\rho$, and the error on the position of the center O' displaced to the new position O'^{*} and expressed in the frame R'. Figure 20 describes the link considering the errors. The induced variation of the angle θ, $\delta\theta$, is not part of the screw because it corresponds to the joint variable.

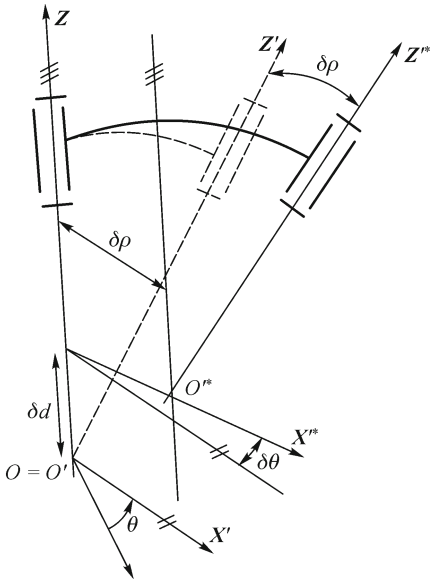

Fig. 20 Link parameters with manufacturing errors

The small rotation can be written as

$$\boldsymbol{\delta\rho} = \delta\rho\cdot\boldsymbol{X}'^{*}, \tag{39}$$

with $\boldsymbol{X}'^{*} = \cos\delta\theta\boldsymbol{X}' + \sin\delta\theta\boldsymbol{Y}'$.

However, since $\delta\theta$ is infinitely small, $\boldsymbol{X}'^{*}$ becomes

$$\boldsymbol{X}'^{*} = \boldsymbol{X}' + \delta\theta\boldsymbol{Y}, \tag{40}$$

and we obtain

$$\delta\boldsymbol{\rho} = \delta\rho\cdot\boldsymbol{X}' + \delta\rho\cdot\delta\theta\cdot\boldsymbol{Y}. \tag{41}$$

Considering only small displacements of the first order, we can write

$$\delta\boldsymbol{\rho} = \delta\rho\cdot\boldsymbol{X}', \tag{42}$$

also

$$\delta\boldsymbol{t} = \boldsymbol{O}'\boldsymbol{O}'^{*} = \delta d\boldsymbol{Z} + \delta\rho\boldsymbol{X}'^{*}. \tag{43}$$

The two latter equations yield

$$\delta\boldsymbol{t} = \delta\rho\boldsymbol{X}' + \delta d(-\sin\rho\boldsymbol{Y}' + \cos\rho\boldsymbol{Z}'). \tag{44}$$

Therefore, the screw of the manufacturing errors of the link *R-R* can be expressed as

$$\$^{S}_{S^*} = \begin{Bmatrix} \delta\boldsymbol{\rho} \\ \delta\boldsymbol{t} \end{Bmatrix} = \begin{Bmatrix} \delta\rho \\ 0 \\ 0 \\ \delta a \\ -\delta d\,\sin\rho \\ \delta d\,\cos\rho \end{Bmatrix}_{R'}. \tag{45}$$

For the different links of the 3-*RRR*, the angle ρ is equal to

$$\begin{aligned}&\text{-The base } (1): \rho = \rho_1 = \pi/2,\\ &\text{-The link } 1k: \rho = \alpha,\\ &\text{-The link } 2k: \rho = \beta,\\ &\text{-And the platform } (2): \rho = \rho_2 = \pi/6.\end{aligned} \tag{46}$$

6.3 Screw of operating errors

The screw of operating error describes the displacement caused by the manufacturing errors. This small displacement is allowed by the joint and represents a deviation from the nominal angle value. Since the base joints are locked by the motors, we assume that the screw of operation error in these joints is zero.

In general, the operating errors corresponding to a joint R can be written as

$$\Im_{s'}^{s*} = \{0\ \ 0\ \ \delta\gamma_{ik}\ \ 0\ \ 0\ \ 0\}_{R'}^{\mathrm{T}}, \tag{47}$$

with i = 1,2,3 and k = A,B,C.

6.4 The loop closure equations

As defined previously in Fig. 18, the mechanism model can be described by two closed loops. The equations solving this model can be detailed as

· For loop I: legs A and B

$$\begin{aligned}&(\Im_1^{1B*} + \Im_{1B*}^{1B}) + (\Im_{1B}^{2B*} + \Im_{2B*}^{2B}) + (\Im_{2B}^{2*} + \Im_{2*}^{2})\\ &+(\Im_2^{2A*} + \Im_{2A*}^{2A}) + (\Im_{2A}^{1A*} + \Im_{1A*}^{1A}) + (\Im_{1A}^{1*} + \Im_{1*}^{1})\\ &= \begin{Bmatrix}0\\0\end{Bmatrix}.\end{aligned} \tag{48}$$

· For loop II: legs A and C

$$\begin{aligned}&(\Im_1^{1C*} + \Im_{1C*}^{1C})(\Im_{1C}^{2C*} + \Im_{2C*}^{2C}) + (\Im_{2C}^{2'*} + \Im_{2'*}^{2})\\ &+(\Im_2^{2A*} + \Im_{2A*}^{2A}) + (\Im_{2A}^{1A*} + \Im_{1A*}^{1A}) + (\Im_{1A}^{1*} + \Im_{1*}^{1})\\ &= \begin{Bmatrix}0\\0\end{Bmatrix}.\end{aligned} \tag{49}$$

Since we consider that the operating errors in the active joints are zero, the screws $\Im_{1A}^{1*}$, $\Im_1^{1B*}$ and $\Im_1^{1C*}$ are zero and Eqs. (48) and (49) can be written as

$$\begin{aligned}&\Im_{1B}^{2B*} + \Im_{2B}^{2*} + \Im_2^{2A*} + \Im_{2A}^{1A*}\\ &= -\Im_{1B*}^{1B} - \Im_{2B*}^{2B} - \Im_{2*}^{2} - \Im_{2A*}^{2A} - \Im_{1A*}^{1A} - \Im_{1*}^{1}.\end{aligned} \tag{50}$$

$$\begin{aligned}&\Im_{1C}^{2C*} + \Im_{1C}^{2'*} + \Im_2^{2A*} + \Im_{2A}^{1A*}\\ &= -\Im_{1C*}^{1C} - \Im_{2C*}^{2C} - \Im_{2'*}^{2} - \Im_{2A*}^{2A} - \Im_{1A*}^{1A} - \Im_{1*}^{1}.\end{aligned} \tag{51}$$

The three first scalar equations in Eqs. (50) and (51) can be written in a vector form as

$$\begin{aligned}&\delta\gamma_{2B}\boldsymbol{Z}_{2B} + \delta\gamma_{3B}\boldsymbol{Z}_{3B} + \delta\gamma_{3A}\boldsymbol{Z}_{3A} + \delta\gamma_{2A}\boldsymbol{Z}_{2A}\\ &= -\delta\alpha_{1B}\boldsymbol{X}_{1B} - \delta\beta_{2B}\boldsymbol{X}_{2B} - \delta\rho_2\boldsymbol{X}_{3B} - \delta\beta_{2A}\boldsymbol{X}_{3A}\\ &\quad -\delta\alpha_{1A}\boldsymbol{X}_{2A} - \delta\rho_1\boldsymbol{X}_{1A}.\end{aligned} \tag{52}$$

$$\begin{aligned}&\delta\gamma_{2C}\boldsymbol{Z}_{2C} + \delta\gamma_{3C}\boldsymbol{Z}_{3C} + \delta\gamma_{3A}\boldsymbol{Z}_{3A} + \delta\gamma_{2A}\boldsymbol{Z}_{2A}\\ &= -\delta\alpha_{1C}\boldsymbol{Z}_{1C} - \delta\beta_{2C}\boldsymbol{X}_{2C} - \delta\rho_2\boldsymbol{X}_{3C} - \delta\rho_2\boldsymbol{X}_{3C}\\ &\quad -\delta\beta_{2A}\boldsymbol{X}_{3A} - \delta\alpha_{1A}\boldsymbol{X}_{2A} - \delta\rho_1\boldsymbol{X}_{1A}.\end{aligned} \tag{53}$$

We get then 6 scalar equations in six unknown operating errors: $\delta\gamma_{2B}$, $\delta\gamma_{3B}$, $\delta\gamma_{3A}$, $\delta\gamma_{2A}$, $\delta\gamma_{2C}$ and $\delta\gamma_{3C}$.

However, the last three scalar equations in Eqs. (50) and (51) yield 6 linear equations, which do not contain the operating errors. These equations represent the six compatibility relations representing the overconstraints of the mechanism.

6.5 Calculation of the orientation errors of the end-effector

Solving Eqs. (52) and (53) yields the operating errors, which can be used to calculate the orientation errors of the platform as follows:

$$\begin{Bmatrix}\delta\boldsymbol{r}\\ \delta\boldsymbol{o}\end{Bmatrix} = \Im_2^{2A*} + \Im_{2A*}^{2A} + \Im_{1A}^{1A*} + \Im_{1*}^{1}, \tag{54}$$

where $\delta\boldsymbol{r}$ is the vector of the rotation error, given by

$$\begin{aligned}\delta\boldsymbol{r} = \begin{bmatrix}\delta r_x\\ \delta r_y\\ \delta r_z\end{bmatrix} &= \delta\gamma_{3A}\mathbf{Z}_{3A} + \delta\beta_{2A}\mathbf{X}_{3A} + \delta\gamma_{2A}\mathbf{Z}_{2A}\\ &\quad + \delta a_{1A}\boldsymbol{X}_{2A} - \delta\rho_1\boldsymbol{X}_{1A}.\end{aligned} \tag{55}$$

For clarity, we can adopt the axis-angle representation to evaluate the error in orientation. The error angle can then be written as

$$\delta\phi = \arccos\left(1/2(\mathrm{tr}(\boldsymbol{M}) - 1)\right), \tag{56}$$

where $\boldsymbol{M} = Rot(\boldsymbol{X}_0,\delta r_x)\cdot Rot(\boldsymbol{Y}_0,\delta r_y)\cdot Rot(\boldsymbol{Z}_0,\delta r_z)$, δr_x, δr_y and δr_z are given by Eq. (55).

The second three scalar equations of the Eq. (54) represent the vector of the SPM center translation. Theoretically, this vector must be zero to ensure the mounting of the mechanism, which represent the six

compatibility equations to be satisfied by the linear manufacturing errors. This problem is not studied in this paper.

6.5.1 Manufacturing errors data:

Since the calculation of the error depends on the configuration of the SPM, we will span the workspace of the SPM by taking 100 orientations of the platform axis $\boldsymbol{Z}_E$ among the set represented by the cone of Fig. 11.

For the manufacturing errors we chose angular values for $\delta\rho$ ranging from 10' to 30'.

The purpose of this study is to test different levels for manufacturing errors and calculate the induced rotation errors of the 3-*RRR* SPM. For each one of the 100 platform orientations, we calculate the errors by taking 1000 random choices of the values of the manufacturing errors corresponding to every link detailed in Eq. (46) and contained in the ranges previously mentioned. The number of possible choices can reach 2^{12} (we have 12 manufacturing errors in Eqs. (52) and (53). It is worth mentioning that choosing a number of error combinations greater than 1000 did not have an effect on the obtained results.

6.5.2 Orientation error of the end-effector:

Figure 21 gives the cumulative distribution of the rotation error for 6 different values of the angular manufacturing error $\delta\rho$. The limit values of the orientation error $\delta\phi$, at a ceiling of 95% confidence interval, are given in column 2 of Table 1. The same table gives the mean values of the overall 10^5 calculated rotation errors. The high obtained values, especially for $\delta\rho = \pm 30'$, are extreme values that have a low probability to happen. This is clearly illustrated by Fig. 22 which represents the rotation errors distribution in the case of $\delta\rho = \pm 30'$. The peak of the curve representing the generalized extreme value distribution used to fit this skew symmetric distribution, is obtained for an error value of 1, 1° which is far away from the 5.5° obtained at 95% of confidence.

In our application and since we imitate the manual movement of the surgeon, we estimate that an error less than 3° at 95% of confidence level, is acceptable. Therefore the manufacturing angular error $\delta\rho = \pm 14'$ can be considered.

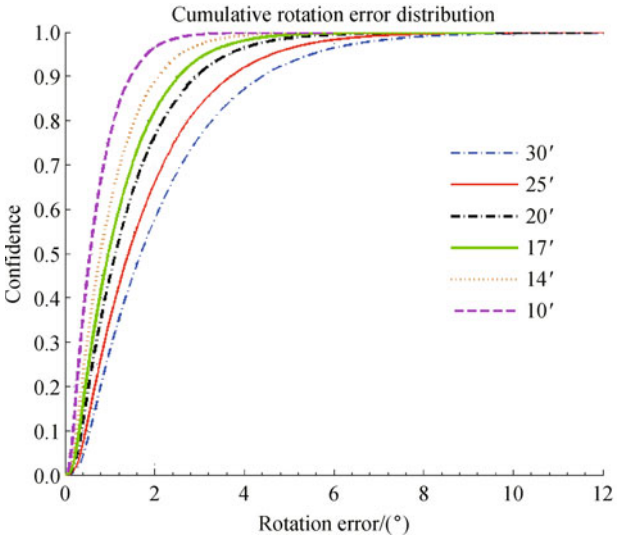

Fig. 21 Rotation error of the platform

Table 1 Characteristics of the rotation error distribution

Manufacturing error/(')	Error at 95% confidence/(°)	Mean value/(°)
10	1.8	0.7
14	2.6	1
17	3.2	1.3
20	3.7	1.5
25	4.6	1.9
30	5.5	2.2

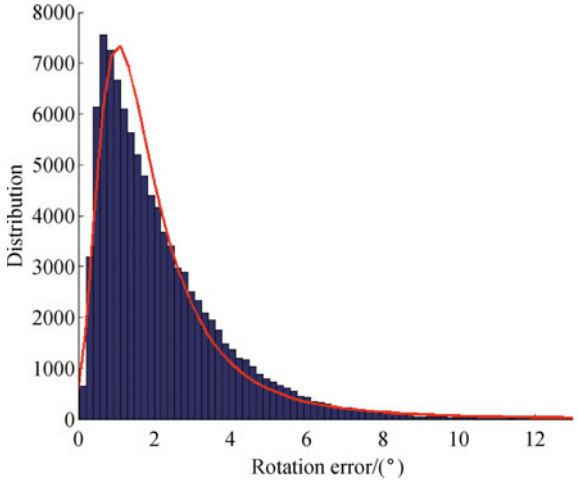

Fig. 22 Rotation error distribution for $\delta\rho = 30'$

7 Conclusions

An optimized design of a haptic device for minimally invasive surgery was presented. The mechanism is based on a spherical parallel architecture optimized to suit the workspace of the anastomosis operation and provide maximum handling dexterity. This workspace was characterized experimentally by a motion capture system recording the movements of an expert performing the surgical task. A multi objective optimization was performed using a genetic algorithm method to identify the optimal geometric parameter of the desired manipulator. The objective functions to be minimized are the

workspace and the dexterity of the SPM. A study of the behavior of the mechanism with respect to manufacturing errors was also detailed. It was shown that an angular manufacturing error range of $\pm 14'$ can yield up to 2.6° of error on the orientation of the end effector.

Acknowledgements This research is supported by the CPER Poitou-Charentes 2007–2013 (program project 10'Images et interactivites'), in partnership with the European Union (FEDER/ERDF, European Regional Development Fund).

References

1. Li T, Payandeh S. Design of spherical parallel mechanisms for application to laparoscopic surgery. Robotica, 2002, 20(2): 133–138
2. Bulca F, Angeles J, Zsombor-Murray P J. On the workspace determination of spherical serial and platform mechanisms. Mechanism and Machine Theory, 1999, 34(3): 497–512
3. Bai S. Optimum design of spherical parallel manipulator. Mechanism and Machine Theory, 2010, 45(2): 200–211
4. Gosselin C, St-Pierre E, Gangné M. On the development of the agile eye. Mechnaical Design, Control Issues and Experimentation. IEEE Robotics & Automation Magazine, 1996, 3(4): 29–37
5. Gosselin C, Lavoie E. On the kinematic design of spherical three-degree-of-freedom parallel manipulators. International Journal of Robotics reaserch. 1993, 12(4): 394–402
6. Bonev I A, Chablat D, Wenger P. Working and assebly modes of the agile eye. In: Proceedings of the IEEE International Conference on Robotics and Automation, 2006, Orlando-Florida, 2317–2322
7. Zanganeh K E, Angeles J. Kinematic isotropy and the optimum design of parallel manipulators. Internatinal Journal of Robotics Reaserch, 1997, 2(4): 16
8. Bonev I A, Gosselin C M. Singularity loci of spherical parallel mechanisms. In: Proceedings of the IEEE International Conference on Robotics and Automation, 2005, 2957–2962
9. Gosselin C, Wang J. Singularity loci of a special class pf spherical three-degree-of-freedom parallel machanisms with revolute actuator. International Journal of Robotic Reaserches, 2002, 21(7): 649–659
10. Wu G, Cavanagh P R. ISB recommendations for standardization in the reporting of kinematic data. Journal of Biomechanics, 1995, 28 (10): 1257–1261
11. Karouia M, Hervé J M. Asymmetrical 3-dof spherical parallel mechanisms. European Journal of Mechanics-A/Solids, 2005, 24(1): 47–57
12. di Gregorio R. A new parallel wrist using only revolute pairs: The 3-RUU wrist. Robotica, 2001, 19(03): 305–309
13. Al-Widyan K, Ma X Q, Angeles J. The robust design of parallel spherical robots. Mechanism and Machine Theory, 2011, 46(3): 335–343
14. Karouia M, Hervé J M. Enumération de mécanismes parallèles sphériaques isostatiques. In: 16ème Congrès Français de Mécanique, 2003, Nice
15. Gleicher M. Retargetting motion to new characters. In: Proceedings of the 25th annual Conference on Computer Graphics and Interactive Techniques, 1998, 33–42
16. Merlet J P. Jacobian, manipualbility, condition number and acuuracy of parallel robots. Journal of Mechanical Design. 2006, 128(1): 199–206
17. Laribi M A, Romdhane L, Zeghloul S. Analysis and dimensional synthesis of the DELTA robot for a prescribed workspace. Mechanism and Machine Theory, 2007, 42(7): 859–870
18. Laribi M A, Mlika A, Romdhane L, Zeghloul S. Criteria optimum design of 3 DOF translational parallel manipulators. In: Proceedings of the 13rd IFToMM World Congress, 2011, Guanajuato